

Magnetic field effects in few-level quantum dots: Theory and application to experiment

Christopher J. Wright, Martin R. Galpin, and David E. Logan

Chemistry Department, Physical & Theoretical Chemistry, Oxford University, South Parks Road, Oxford OX1 3QZ, United Kingdom

(Received 3 August 2011; published 16 September 2011)

We examine several effects of an applied magnetic field on Anderson-type models for both single- and two-level quantum dots, and we make direct comparison between numerical renormalization group (NRG) calculations and recent conductance measurements. On the theoretical side, the focus is on magnetization, single-particle dynamics, and zero-bias conductance, with emphasis on the universality arising in strongly correlated regimes, including a method to obtain the scaling behavior of field-induced Kondo resonance shifts over a very wide field range. NRG is also used to interpret recent experiments on spin- $\frac{1}{2}$ and spin-1 quantum dots in a magnetic field, which we argue do not wholly probe universal regimes of behavior, and the calculations are shown to yield good qualitative agreement with essentially all features seen in experiment. The results capture in particular the observed field dependence of the Kondo conductance peak in a spin- $\frac{1}{2}$ dot, with quantitative deviations from experiment occurring at fields in excess of ~ 5 T, indicating the eventual inadequacy of using the equilibrium single-particle spectrum to calculate the conductance at finite bias.

DOI: [10.1103/PhysRevB.84.115308](https://doi.org/10.1103/PhysRevB.84.115308)

PACS number(s): 72.15.Qm, 73.63.Kv, 71.27.+a

I. INTRODUCTION

Understanding electronic transport in quantum dots remains a major challenge for theorists working on correlated electron systems. Conductance at low energies is often dominated by one of a number of Kondo effects,¹ in which the strong localized interactions on the dot(s) induce nontrivial many-body physics. Over the years, a wide range of such Kondo effects have been predicted and observed, in single and multiple quantum dot devices of various geometries.^{2–6}

Here we consider a single quantum dot, tunnel-coupled to two leads^{7–11} in an effective one-channel fashion. While the dot will in general hold many electrons in its quantized levels, only those close to the Fermi level contribute in practice to electronic transport provided the mean level spacing is sufficiently large, and the rest can be neglected with relative impunity. Typically just one level is important, but occasionally one observes the case of two relevant levels, where the physics is richer—including, e.g., a quantum phase transition between Fermi liquid and underscreened Kondo phases,^{12–26} which has been observed in several experimental guises.^{27–29}

We present and examine critically a number of results falling under the umbrella of magnetic field (B) effects in these single- and two-level quantum dots, the appropriate models for which are specified in Sec. II. The paper consists of two related parts. In the first (Secs. III and IV), using mainly Wilson's numerical renormalization group (NRG) method,^{30–32} we consider magnetization, single-particle dynamics, and the zero-bias conductance, with emphasis on the universality and scaling behavior arising in the strongly correlated regimes of the models.

Even for single-level quantum dots described by an Anderson impurity model,^{1,33} there are still open questions regarding single-particle dynamics in the presence of a magnetic field, our primary concern being the field-induced Kondo peak splitting in the equilibrium single-particle spectrum. This has been analyzed by a number of authors and techniques,^{34–42} but the results are not in complete agreement.^{34,36,37,43} We show that there exists an algorithm by which NRG can obtain the

universal behavior over many orders of magnitude of field strength, but that, eventually, even the most accurate NRG calculations cannot completely resolve the universal splitting at very large fields. The corresponding situation for the two-level model is considered in Sec. IV B. We also obtain the field and temperature (T) dependence of the zero-bias conductance, and for $T = 0$ in particular generalize the Luttinger integral analysis of Ref. 24 to encompass a finite magnetic field, leading to an exact result for the conductance for any field, and insight into the rather subtle differences between the limits $B = 0$ and $B \rightarrow 0$ for the underscreened triplet phase of the model.

In the second part of the paper (Sec. V), we turn to a comparison with experiment. Two recent sets of conductance measurements on quantum dots in a magnetic field are considered, from the groups of Kogan⁴⁴ (on an effective one-level dot) and Goldhaber-Gordon⁴³ (on both effective one- and two-level systems). From comparison to NRG results, we are able to determine reliable bare model parameters for the Anderson-type (as opposed to Kondo) models considered in Secs. II–IV, as relevant to experiment. With these, our NRG calculations are shown to yield very good qualitative agreement with essentially all features observed in both experiments.^{43,44} In particular, we show that theory can in fact explain the evolution of the field-induced splitting of the Kondo conductance peak observed in Ref. 44—including a simple explanation for an observed crossing in the peak splittings of two different quantum dots. The agreement is essentially quantitative up to field strengths of around a couple of Kondo scales, but beyond that, our calculations deviate from the experimental data. This reinforces results from a recent study using the scattering states NRG⁴⁵ and earlier renormalized perturbation theory and NRG calculations,^{38,46} showing that the commonly used approximation of calculating the source-drain bias dependence of the conductance from the equilibrium spectrum is unsuitable for making quantitative comparisons to experiment sufficiently far out of equilibrium. Indeed, until more progress in nonequilibrium theory is made, we suggest that experiments should instead aim to make

comparison with the magnetic field dependence of the zero-bias conductance.

II. MODELS

Each model considered in this work consists of a single interacting quantum dot region, tunnel coupled to a pair of noninteracting metallic leads. As mentioned above, we focus on the situation in which the mean level spacing of the dot is sufficiently large compared to the dot-lead tunneling strength that generally only one, or occasionally two, levels are involved in transport.

When just one dot level is relevant, the standard model is the Anderson impurity model (AIM).^{7,8,33} Here the dot itself is described by

$$\hat{H}_D^{\text{AIM}} = \sum_{\sigma} \left(\epsilon_{1\sigma} + \frac{1}{2} U \hat{n}_{1-\sigma} \right) \hat{n}_{1\sigma}, \quad (1)$$

where $\hat{n}_{1\sigma} = d_{1\sigma}^{\dagger} d_{1\sigma}$ counts the σ spin electrons on the dot level, U is the on-level Coulomb repulsion/charging energy, and $\epsilon_{1\sigma} = \epsilon_1 - \sigma h$ is the level energy. The latter includes a Zeeman coupling to an external magnetic field B with $h = \frac{1}{2} g \mu_B B$ and $\sigma = +/ -$ for \uparrow / \downarrow -spin electrons. In the case of two relevant dot levels, the dot Hamiltonian is naturally more complex. We choose to work with the following two-level model (2LM):

$$\hat{H}_D^{2\text{LM}} = \sum_{i,\sigma} \left(\epsilon_{i\sigma} + \frac{1}{2} U \hat{n}_{i-\sigma} \right) \hat{n}_{i\sigma} + U' \hat{n}_1 \hat{n}_2 - J_H \hat{\mathbf{s}}_1 \cdot \hat{\mathbf{s}}_2, \quad (2)$$

which has previously been shown to capture the key physics of two-level quantum dots in the absence of a magnetic field.²⁴ Here $\hat{n}_i = \sum_{\sigma} \hat{n}_{i\sigma}$ is the total number operator for level i ($=1,2$), and $\hat{\mathbf{s}}_i$ is the local spin operator with components $\hat{s}_i^{\alpha} = \sum_{\sigma,\sigma'} d_{i\sigma}^{\dagger} \sigma_{\sigma\sigma}^{\alpha} d_{i\sigma'}$ ($\sigma_{\sigma\sigma'}$ are the Pauli spin- $\frac{1}{2}$ matrices). In addition to the on-level Coulomb repulsion U (taken to be identical for levels 1 and 2 for simplicity), the model includes an interlevel Coulomb repulsion U' plus a ferromagnetic (Hund's rule) exchange coupling of the spins of the two levels, parametrized by J_H .

In each case, the dot Hamiltonian is supplemented by coupling to two equivalent, noninteracting ‘‘left’’ and ‘‘right’’ leads, themselves described by $\hat{H}_L = \sum_{\nu} \sum_{\mathbf{k},\sigma} \epsilon_{\mathbf{k}} a_{\mathbf{k}\nu\sigma}^{\dagger} a_{\mathbf{k}\nu\sigma}$ ($\nu = L, R$), where the most general tunnel coupling to the leads is of form $\hat{H}_T = \sum_{\nu} \sum_{i,\mathbf{k},\sigma} V_{i\mathbf{k}\nu} (d_{i\sigma}^{\dagger} a_{\mathbf{k}\nu\sigma} + \text{H.c.})$ (the sum over level index i involving just $i = 1$ in the case of the AIM). The L and R lead chemical potentials are μ_L and μ_R , respectively, such that for $\mu_L \neq \mu_R$ a nonzero current flows.

Analyzing the interacting models out of equilibrium is a formidable task (see, e.g., Ref. 47 for a recent discussion), and in practice we consider the equilibrium situation. This has an immediate benefit, for the AIM Hamiltonian then reduces exactly to an effective one-lead model by defining $c_{\mathbf{k}\sigma} = (V_{i\mathbf{k}L} a_{\mathbf{k}L\sigma} + V_{i\mathbf{k}R} a_{\mathbf{k}R\sigma}) / V_{i\mathbf{k}}$ with $V_{i\mathbf{k}}^2 = V_{i\mathbf{k}L}^2 + V_{i\mathbf{k}R}^2$ (with $i = 1$), since the corresponding orthogonal combination of lead states is entirely decoupled from the dot. The two-level dot Hamiltonian under this transformation does not generally separate so pristinely: except in the special case of $V_{i\mathbf{k}L} =$

$V_{i\mathbf{k}} \cos \theta$, $V_{i\mathbf{k}R} = V_{i\mathbf{k}} \sin \theta$, the dot remains coupled to two leads.¹⁵ However, over a wide range of parameter space, the second lead couples sufficiently weakly that it may in practice be neglected on energy scales of practical interest.¹⁵ As such, for both the AIM and 2LM we work with the effective one-lead description embodied in

$$\hat{H}_L + \hat{H}_T = \sum_{\mathbf{k},\sigma} \epsilon_{\mathbf{k}} c_{\mathbf{k}\sigma}^{\dagger} c_{\mathbf{k}\sigma} + \sum_{i=1}^N \sum_{\mathbf{k},\sigma} V_{i\mathbf{k}} (d_{i\sigma}^{\dagger} c_{\mathbf{k}\sigma} + \text{H.c.}) \quad (3)$$

with $N = 1$ for the AIM and $N = 2$ for the 2LM.

We consider the standard case¹ of a symmetric, flat-band lead of half-width D and density of states per orbital $\rho_0 = 1/(2D)$, and we take $V_{i\mathbf{k}} \equiv V$. The dot-lead coupling is then embodied in the hybridization strength $\Gamma = \pi \rho_0 |V|^2$ (with $\rho = \mathcal{N} \rho_0$ the total density of states and $\mathcal{N} \rightarrow \infty$ the number of lead orbitals). When presenting results, we use dimensionless parameters defined in terms of Γ , viz.,

$$\tilde{\epsilon}_i = \frac{\epsilon_i}{\Gamma}, \quad \tilde{U} = \frac{U}{\Gamma}, \quad \tilde{U}' = \frac{U'}{\Gamma}, \quad \tilde{J}_H = \frac{J_H}{\Gamma}, \quad \tilde{h} = \frac{h}{\Gamma}. \quad (4)$$

The bandwidth D is naturally taken to be the largest energy scale in the problem, and for our NRG calculations in practice we take $D/\Gamma = 100$.

To study the models described above, the central quantities of interest are the dot Green functions $G_{ij;\sigma}(\omega; h)$ [$\leftrightarrow G_{ij;\sigma}(t; h) = -i\theta(t)\langle\{d_{i\sigma}(t), d_{j\sigma}^{\dagger}(0)\}\rangle$] with associated spectral density $D_{ij;\sigma}(\omega; h) = -\frac{1}{\pi} \text{Im} G_{ij;\sigma}(\omega; h)$ [$\theta(t)$ denotes the unit step function]. In the absence of an applied magnetic field, $G_{ij;\uparrow}(\omega; 0) = G_{ij;\downarrow}(\omega; 0)$, while for any finite h the \uparrow - and \downarrow -spin Green functions are naturally distinct. In addition to these spin-resolved quantities, we will later make use of their spin-summed analogs, in particular the spin-summed spectrum

$$D_{ij}(\omega; h) = \frac{1}{2} \sum_{\sigma} D_{ij;\sigma}(\omega; h). \quad (5)$$

Moreover, in the case of the 2LM some of the physics is better described in terms of the symmetrized combinations of dot orbitals,²⁴

$$d_{e\sigma} = \frac{1}{\sqrt{2}}(d_{1\sigma} + d_{2\sigma}), \quad d_{o\sigma} = \frac{1}{\sqrt{2}}(d_{1\sigma} - d_{2\sigma}) \quad (6)$$

from which follow the ‘‘even-even’’ and ‘‘odd-odd’’ Green functions:

$$G_{ee;\sigma}(\omega) = \frac{1}{2} [G_{11;\sigma}(\omega) + G_{22;\sigma}(\omega) + 2G_{12;\sigma}(\omega)], \quad (7)$$

$$G_{oo;\sigma}(\omega) = \frac{1}{2} [G_{11;\sigma}(\omega) + G_{22;\sigma}(\omega) - 2G_{12;\sigma}(\omega)]. \quad (8)$$

The connection between theory and experiment is made via the zero-bias differential conductance, $G_c^0(T)$. For the models considered above, this is obtained exactly from the Meir/Wingreen approach,⁹ which gives

$$G_c^0(T; h) = \frac{2e^2}{h} G_0 \int_{-\infty}^{+\infty} d\omega \frac{-\partial f(\omega)}{\partial \omega} N \pi \Gamma D_{ss}(\omega; h). \quad (9)$$

Here $f(\omega) = (e^{\omega/T} + 1)^{-1}$ ($k_B \equiv 1$) is the Fermi function, and $D_{ss}(\omega; h) = \frac{1}{N} \sum_{i,j} D_{ij}(\omega; h)$ is the spectral density of the fully symmetric impurity channel [i.e., $D_{11}(\omega; h)$ for the AIM and $D_{ee}(\omega; h)$ for the 2LM]. The dimensionless prefactor

$G_0 = \sin^2 2\theta$ reflects the relative coupling asymmetry to the right and left leads and is maximal, $G_0 = 1$, for equal couplings.²⁴

As alluded to above, present methods cannot give exact results for the nonequilibrium situation of a finite source-drain bias between the leads. While recent progress has been made in addressing this (see, e.g., Refs. 45, 47, and 48), the methods used are much more computationally intensive and thus we make the standard approximation of neglecting the V_{sd} dependence of the impurity self-energy. The result is that

$$\frac{G_c(T, V_{sd}; h)}{(2e^2/h)G_0} = - \int_{-\infty}^{+\infty} d\omega \left[\lambda \frac{\partial f_L(\omega)}{\partial \omega} + (1 - \lambda) \frac{\partial f_R(\omega)}{\partial \omega} \right] N\pi\Gamma D_{ss}(\omega; h), \quad (10)$$

where $f_\nu(\omega) = f(\omega - \mu_\nu)$ with $\mu_L = \lambda e V_{sd}$ and $\mu_R = -(1 - \lambda)e V_{sd}$. The quantity $\lambda \in (0, 1)$ controls the partitioning of the voltage split eV_{sd} between the two leads, with $\lambda = \frac{1}{2}$ corresponding to a symmetric voltage drop. In Sec. V, we use Eq. (10) to interpret a number of recent experimental results, where in particular we discuss critically the agreement between this quasiequilibrium approximation and experiment.

Finally, our numerics are obtained from the full density matrix (FDM)^{49,50} formulation of the NRG,^{30–32} using the Oliveira discretization scheme⁵¹ and a generalization of the self-energy method of Bulla *et al.*⁵² We find it sufficient to keep ~ 4000 states per NRG iteration, and employ an NRG discretization parameter $\Lambda = 3$.

III. ZERO-FIELD PHYSICS AND LOW-ENERGY EFFECTIVE MODELS

To put our finite-field results in context, we consider briefly the zero-field physics of the two models; starting with the AIM, which at zero field is well understood by a range of complementary techniques (see, e.g., Ref. 1).

The AIM exhibits local Fermi liquid behavior for all $\Gamma > 0$, as reflected in the RG description by a single stable fixed point (FP): the strong-coupling (SC) fixed point.^{30,31} For fixed U/Γ , the dot occupancy $n_1 = \langle \hat{n}_1 \rangle$ increases continuously with decreasing ϵ_1 , starting close to $n_1 \simeq 0$ when $\epsilon_1/\Gamma \gg 1$, and tending to a maximum of 2 when $(\epsilon_1 + U)/\Gamma \ll 1$. At the point $\epsilon_1 = -U/2$, the model is invariant under a particle-hole (p-h) transformation¹ and hence $n_1 = 1$ precisely.

When charge fluctuations are suppressed by a large $U/\Gamma \gg 1$, the dot occupancy tends toward integer values, increasing more or less stepwise as ϵ_1 is decreased (under a gate voltage in practice, $\epsilon_1 \propto V_{\text{gate}}$). In the singly occupied regime ($n_1 \simeq 1$), the AIM reduces under a Schrieffer-Wolff transformation⁵³ of Eqs. (1) and (3) to a low-energy effective Kondo model: defining a p-h asymmetry parameter $\eta = (1 + 2\epsilon_1/U)$, for a fixed $-1 < \eta < 1$ and $\tilde{U} = U/\Gamma \gg 1$ this yields

$$\hat{H}_K = \sum_{\mathbf{k}, \sigma} \epsilon_{\mathbf{k}} c_{\mathbf{k}\sigma}^\dagger c_{\mathbf{k}\sigma} + J\hat{\mathbf{s}} \cdot \hat{\mathbf{S}}(0) + K \sum_{\sigma} f_{0\sigma}^\dagger f_{0\sigma}, \quad (11)$$

where $\hat{\mathbf{s}}$ is a spin- $\frac{1}{2}$ operator describing the dot spin, $\hat{\mathbf{S}}^\alpha(0) = \sum_{\sigma, \sigma'} f_{0\sigma}^\dagger \sigma_{\sigma\sigma'}^\alpha f_{0\sigma'}$ is the conduction band/lead spin density at the dot, and $f_{0\sigma} = \frac{1}{N} \sum_{\mathbf{k}} c_{\mathbf{k}\sigma}$. The Kondo exchange coupling

J and potential scattering strength K are given in terms of the original model parameters by

$$\rho_0 J = \frac{8}{\pi \tilde{U}} \frac{1}{1 - \eta^2}, \quad \rho_0 K = \frac{2}{\pi \tilde{U}} \frac{\eta}{1 - \eta^2}, \quad (12)$$

such that at p-h symmetry ($\eta = 0$) the potential scattering $K = 0$. Away from p-h symmetry, potential scattering is nonvanishing, but, from Eq. (12), $K/J = \eta/4$ and hence for fixed η the model is characterized by a single dimensionless parameter $\rho_0 J$. This in turn means that for a given η , all AIMs in the strongly interacting $\tilde{U} \gg 1$ regime map onto the same low-energy effective Hamiltonian, and thus exhibit universal scaling of their physical properties in terms of the low-energy Kondo scale $T_K \sim D \exp[-1/(\rho_0 J)]$.¹

The physics of the 2LM is naturally more complicated. We refer the reader to Ref. 24 for detailed discussion, and merely summarize the key points here. When considering the model as a function of the level energies ϵ_1 and ϵ_2 , it is more convenient to work with

$$x = \epsilon_1 + \frac{1}{2}U + U', \quad y = \epsilon_2 + \frac{1}{2}U + U', \quad (13)$$

since it can be shown that the model is p-h symmetric when $x = 0 = y$, and that its phase diagram is symmetric under reflection in the lines $y = \pm x$.²⁴ That the phase diagram itself is nontrivial reflects the occurrence now of two stable FP's: the SC FP again, and the underscreened spin-1 (USC) FP of Nozières and Blandin.⁵⁴ As for the AIM, the SC phase is a local Fermi liquid, while the USC phase is a singular Fermi liquid^{24,55} characterized by a free spin- $\frac{1}{2}$ on the dot with a $\ln 2$ residual entropy.

Close to p-h symmetry ($x = 0 = y$), the dot levels are each singly occupied, and in the absence of coupling to the lead naturally form a spin-triplet. On coupling to the lead, this spin-1 is reduced to an effective spin- $\frac{1}{2}$ by the underscreened Kondo effect,⁵⁴ whence a finite region surrounding the p-h symmetric point belongs to the USC phase. On moving further away from p-h symmetry [in any direction in the (x, y) plane], the model eventually undergoes a quantum phase transition to the SC phase (see Fig. 5 of Ref. 24). The transition is of Kosterlitz-Thouless (KT) type,²⁴ the Kondo scale in the SC phase vanishing exponentially as the boundary to the USC phase is approached. This holds generically except at points of special symmetry (specifically along the line $y = x$, where the transition becomes first-order²⁴).

The effective low-energy model “deep” in the underscreened triplet regime can be obtained by Schrieffer-Wolff on the 2LM, Eqs. (2) and (3), valid formally for $U/\Gamma \gg 1$ with fixed J_H/U and U'/U . The resulting model is spin-1 Kondo with potential scattering,²⁴ of the same form as Eq. (11) but with $\hat{\mathbf{s}}$ now a spin-1 operator and J, K given by

$$\rho_0 J(x, y) = \frac{4}{\pi(\tilde{U} + \frac{1}{2}\tilde{J})} \left[\frac{1}{1 - \eta(x)^2} + \frac{1}{1 - \eta(y)^2} \right], \quad (14a)$$

$$\rho_0 K(x, y) = \frac{2}{\pi(\tilde{U} + \frac{1}{2}\tilde{J})} \left[\frac{\eta(x)}{1 - \eta(x)^2} + \frac{\eta(y)}{1 - \eta(y)^2} \right], \quad (14b)$$

where (with $z = x$ or y) the asymmetry is

$$\eta(z) = \frac{2z}{U + \frac{1}{2}J_H}. \quad (15)$$

The characteristic Kondo scale deep in the USC phase is⁵⁶ $T_K^{S=1} \sim D \exp[-1/(\rho_0 J)]$ (i.e., has the same exponential dependence on $\rho_0 J$ as for the spin- $\frac{1}{2}$ case).

In direct analogy to the AIM, the ratio of K to J is a function solely of the asymmetries, conveniently expressed in terms of a quantity $\eta(x, y)$:

$$\eta(x, y) = \frac{2K(x, y)}{J(x, y)} = \frac{\eta(x) + \eta(y)}{2 - \frac{[\eta(x) - \eta(y)]^2}{1 - \eta(x)\eta(y)}}. \quad (16)$$

Sufficiently deep in the USC phase, one thus expects physical properties of the 2LM to be universal in $T/T_K^{S=1}$ for fixed $\eta(x, y)$, as considered further in Sec. IV.

IV. FIELD-DEPENDENT STATICS AND DYNAMICS

We now turn to our main focus: the effect of an applied magnetic field on the AIM and 2LM. While much is already known for the AIM, certain aspects of its dynamics in a magnetic field^{34–41} have not been fully understood, and in Sec. IV B we present NRG results to clarify the situation. The 2LM model has been less widely studied, and we consider it in somewhat more detail.

A. Magnetization

It is first instructive to consider the magnetization for level i , here defined by

$$m_i(h) = \langle \hat{n}_{i\uparrow} \rangle - \langle \hat{n}_{i\downarrow} \rangle \quad (17)$$

$$= \int_{-\infty}^0 d\omega [D_{ii,\uparrow}(\omega) - D_{ii,\downarrow}(\omega)]. \quad (18)$$

This can be determined accurately using the FDM-NRG,^{32,49,50} the complete Fock space approach circumventing known problems arising in the original NRG.^{34,35}

Figure 1 shows the total dot magnetization $m(h) = m_1(h)$ versus $\log(h/T_K)$ for the symmetric AIM with $\tilde{U} = 50$ and $\tilde{\epsilon} = -\frac{1}{2}\tilde{U}$.⁵⁷ The accuracy of the FDM-NRG is confirmed by the clear agreement with the exact result known from the Bethe ansatz⁵⁶ for the Kondo model. At a field $h \sim T_K$, the

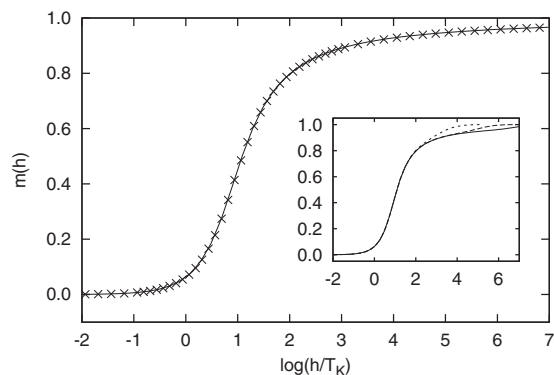


FIG. 1. Magnetization of the AIM vs h/T_K . Main: $\tilde{U} = -2\tilde{\epsilon} = 50$. Comparison between FDM-NRG results (crosses) calculated via Eq. (17), and the Bethe ansatz result⁵⁶ (line) for the Kondo Model. Inset: $\tilde{U} = -2\tilde{\epsilon} = 30$ (solid), 20 (long dash), and 10 (short dash) corresponding to $T_K/\Gamma \sim 1.8 \times 10^{-6}, 8.0 \times 10^{-5}$, and 3.1×10^{-3} . Deviations from universality occur for $h \gtrsim O(\Gamma)$.

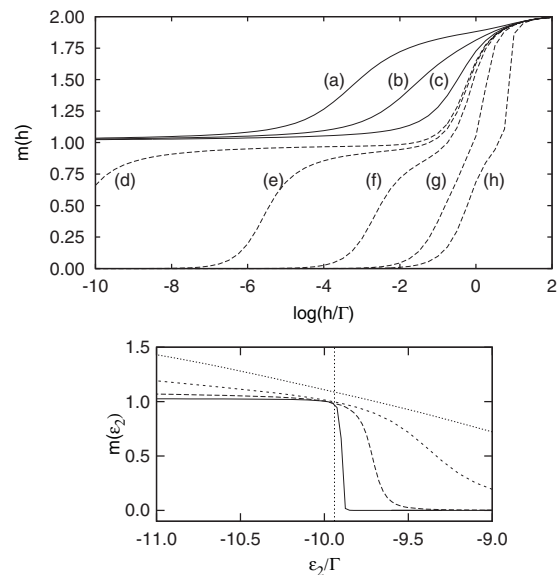


FIG. 2. Upper: Total magnetization $m(h) = m_1(h) + m_2(h)$ of the 2LM with $\tilde{U} = 2\tilde{U}' = 4\tilde{J}_H = 20$, $\tilde{\epsilon}_1 = -\frac{1}{2}\tilde{U} - \tilde{U}' = -20$, and $\tilde{\epsilon}_2 =$ (a) -20 , (b) -12 , (c) -10.5 , (d) -9.9 , (e) -9.8 , (f) -9.5 , (g) -8 , and (h) -2 . At zero field, (a)–(c) correspond to the USC phase; here an infinitesimal field polarizes the underscreened impurity moment. For larger ϵ_2 , the system is in the SC phase at zero field, and $m(h \rightarrow 0) \rightarrow 0$. Lower: Magnetization near the crossover for $\tilde{h} = 10^{-10}$ (solid), 10^{-4} (long dashed), 10^{-2} (short dashed), and 10^{-1} (dotted). The $h = 0$ transition is marked by a dotted vertical line at $\tilde{\epsilon}_{2c} = -9.94$. For $h \rightarrow 0$, m jumps discontinuously at $\tilde{\epsilon}_{2c}$, while for finite fields this step is smeared.

magnetization rises rapidly from its zero field (Kondo-screened) value $m(0) = 0$, before turning over to a slow asymptotic approach to saturation of form $m(h) \sim 1 - [2 \ln(h/T_K)]^{-1}$. The inset to Fig. 1 gives results for $\tilde{U} = 30, 20$, and 10 , showing the inevitable deviation from the universal Kondo magnetization curve at sufficiently high fields $h \gtrsim O(\Gamma)$.

We now compare this behavior to that of the two-level model of Eq. (2). The basic physics now reflects the destruction of the quantum phase transition occurring for $h = 0$, and its replacement by a smooth crossover. In terms of FPs, the spin symmetry breaking associated with the magnetic field renders the USC fixed point unstable for all $h \neq 0$, and so ultimately *all* NRG flows tend toward a SC fixed point (now supplemented by spin-dependent potential scattering).

Figure 2 (upper) shows the total dot magnetization $m(h) = m_1(h) + m_2(h)$ for $\tilde{U} = 2\tilde{U}' = 4\tilde{J}_H = 20$ and with fixed $\epsilon_1 = -\frac{1}{2}U - U'$ [i.e., $x = 0$, see Eq. (13)], upon increasing ϵ_2 (or y) from its p-h symmetric value. In the following, it is useful to bear in mind that on increasing ϵ_2 at *zero field*, the model undergoes the quantum phase transition from USC to SC at a critical $\tilde{\epsilon}_{2c} \simeq -9.94$.

Curves (a)–(c) in Fig. 2 correspond to $\epsilon_2 < \epsilon_{2c}$ and hence the USC phase at $h = 0$. At finite field, these curves show $m(h) \rightarrow 1$ as $h \rightarrow 0$: an infinitesimal field fully polarizes the free spin- $\frac{1}{2}$ local moment associated with the USC fixed point (for $h = 0$ identically, by contrast, the magnetization vanishes by symmetry). On increasing h , the magnetization increases

monotonically, crossing over toward $m(h) = 2$ on the scale $h \sim T_K^{S=1}$ as the field destroys the underscreened Kondo effect and singles out the $S_z = +1$ component of the dot triplet state.⁵⁸ As shown in Ref. 24, $T_K^{S=1}$ increases upon moving away from the center of the USC phase, hence the higher field required to destroy the underscreened Kondo effect for (c) compared to (a).

For larger level separations, $\epsilon_2 > \epsilon_{2c}$ [curves (d)–(h)], the zero-field phase is SC. Here the low-field behavior more closely resembles that of Fig. 1. At zero field, the dot is fully screened by the lead and remains essentially so until h on the order of the SC phase Kondo scale, T_K , above which the spin- $\frac{1}{2}$ Kondo effect is progressively destroyed, and $m(h)$ crosses over to $m(h) \sim 1$ associated with a spin-polarized spin- $\frac{1}{2}$ on the dot. As in curves (a)–(c), increasing the field further then causes a second marked increase in $m(h)$ when the $S_z = +1$ component of the two-electron triplet state is favored.

Figure 2 (lower) shows the magnetization at various fixed values of h/Γ as a function of $\tilde{\epsilon}_2$ (focusing on the vicinity of the zero-field transition at $\tilde{\epsilon}_{2c}$). At any finite field, the magnetization decreases monotonically with increasing $\tilde{\epsilon}_2$, and as $h/\Gamma \rightarrow 0$ the curve approaches the step function $m(\epsilon_2) \rightarrow \theta(\tilde{\epsilon}_{2c} - \tilde{\epsilon}_2)$.¹⁹ In the absence of the field, however, the magnetization naturally vanishes, and hence the limit of $h \rightarrow 0^+$ and $h = 0$ are quite distinct.

As for the spin- $\frac{1}{2}$ Kondo effect in Fig. 1, the magnetization deep in the USC phase (where the low-energy effective model is spin-1 Kondo) is a universal function of $h/T_K^{S=1}$. Figure 3 illustrates scaling of the magnetization for $\tilde{U} = 2\tilde{U}' = 4\tilde{J}_H = 30, 20,$ and 15 at the p-h symmetric point $(x, y) = (0, 0)$ where $\langle \hat{n}_i \rangle = 1$ for $i \in \{1, 2, e, o\}$ [see Eq. (6)]. The main figure shows $m(h)$, the total impurity magnetization. Results for different values of the bare parameters clearly display scaling, onto a different universal form than for the AIM.^{56,59}

Figure 3 (inset) shows also the magnetization of the even and odd impurity orbitals [such that $m(h) = m_e(h) + m_o(h)$] for the $\tilde{U} = 20$ case. The o orbital is clearly polarized to a greater extent than the e orbital by an infinitesimal field, and

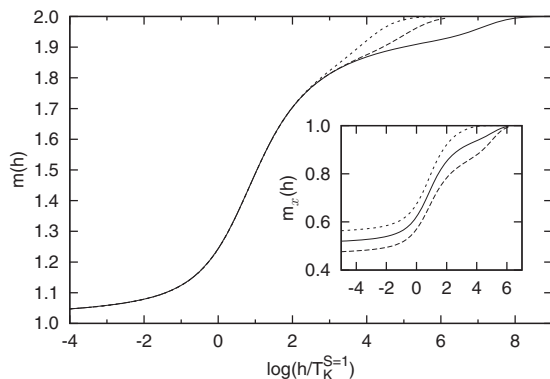


FIG. 3. Magnetization $m(h/T_K^{S=1})$ for the two-level model at p-h symmetry ($\epsilon_1 = \epsilon_2 = -\frac{U}{2} - U'$), deep in the USC phase. $\tilde{U} = 2\tilde{U}' = 4\tilde{J}_H = 30$ (solid), 20 (long dash), and 15 (short dash), corresponding to $T_K^{S=1}/\Gamma = 1.0 \times 10^{-6}, 7.7 \times 10^{-5},$ and 6.8×10^{-4} . As with the AIM, $m(h/T_K^{S=1})$ exhibits universal scaling.^{56,59} Inset: Comparison of $m_x(h)$, $x \in \{1, e, o\}$ (solid, long dash, short dash) for the $\tilde{U} = 20$ case.

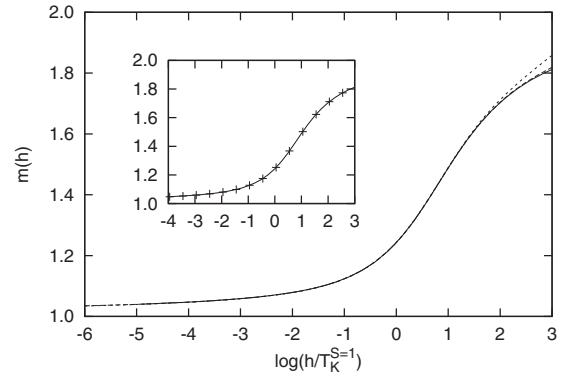


FIG. 4. Magnetization away from p-h symmetry, deep in the USC phase. Main: $m(h) = m_1(h) + m_2(h)$ for the same systems as Fig. 3 but with $\eta(x) = 0$ and $\eta(y) = 0.5$. Clear universality is observed. Inset: The $\tilde{U} = 30$ case on the $y = -x$ line, for $x = 0$ (line) and $x/\Gamma = -6$ (crosses). The resultant universal $m(h)$ is found to be the same in *both* cases, i.e., to be independent of asymmetry.

$m_o(h)$ reaches saturation more quickly than $m_e(h)$ [or indeed $m_1(h)$]. This reflects the fact that the o orbital does not couple directly to the conduction band,²⁴ only interacting with it via the e orbital, which couples directly, the o orbital as such contributing more to the local moment than the e orbital.

The situation deep in the USC phase, but away from p-h symmetry, is illustrated in Fig. 4. As mentioned in Sec. III, universal behavior of $m(h)$ is expected for systems with different bare parameters, at least for fixed asymmetry $\eta(x, y)$ [i.e. from Eq. (15) the same ratio of potential scattering K to Kondo coupling J]. To this end, consider first the line $y = -x$ for *all* points on which $\eta(x, y) = 0$ [Eqs. (16) and (15)]. Figure 4 (inset) shows the universal $m(h)$ at the p-h symmetric point $x = 0 = -y$ (line) considered also in Fig. 3, compared to that obtained some distance away from p-h symmetry at $x = 6\Gamma = -y$ (crosses). The two scaling curves clearly coincide.

The main panel of Fig. 4 illustrates universality for nonvanishing asymmetry, showing $m(h)$ versus $h/T_K^{S=1}$ for the same $\tilde{U} = 2\tilde{U}' = 4\tilde{J}_H$ values as Fig. 3, but now with $\eta(x) = 0$ and $\eta(y) = 0.5$ [i.e., $\eta(x, y) \simeq 0.29$]. The three curves scale perfectly in the universal regime, beginning to deviate only at high fields, $h \sim O(\Gamma)$. Moreover, the resultant universal $m(h)$ is found numerically to be identical to that arising for $\eta(x, y) = 0$, and as such thus appears to be *independent* of asymmetry $\eta(x, y)$, a result we have further confirmed for a wide range of η values.

B. Field-dependent dynamics

We turn now to the field dependence of single-particle dynamics for the AIM and 2LM. Much is already known^{34–42} about the former case, but it serves as a useful comparison to the 2LM and both are experimentally relevant. The spin-resolved impurity spectrum is first considered, with a twofold focus: the field-induced redistribution of weight in the Hubbard satellites, and the shift of the spectral maximum from zero.

Figure 5 shows results for $D_{s\sigma; \downarrow}(\omega; h)$ and a range of fields $h \geq 0$, for both the AIM (inset) and the 2LM. The level energies and interaction strengths have been chosen so that both models are deep in the Kondo regime (for the AIM)

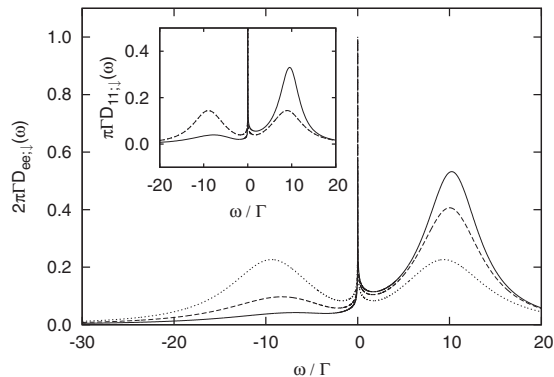


FIG. 5. Redistribution of spectral weight in the Hubbard bands. Main: 2LM with $\tilde{U} = 2\tilde{U}' = 4\tilde{J}_H = 20$ at p-h symmetry, with $h/\omega_K^{S=1} = 0$ (dotted), 1×10^{-6} (dashed), and 1 (solid), $\omega_K^{S=1}$ being the Kondo scale defined as the HWHM of the zero-field Kondo resonance. Inset: AIM with $\tilde{U} = 20$ also at p-h symmetry with $h/\omega_K = 0$ (dotted line), 1×10^{-6} (dashed), and 1 (solid). The result for $h/\omega_K = 1 \times 10^{-6}$ is coincident with that for zero field on the scale shown.

or underscreened triplet (2LM), and are p-h symmetric [such that $D_{ss;\uparrow}(\omega; h) = D_{ss;\downarrow}(-\omega; h)$]. In each case, the familiar three-peak structure is evident: upper and lower Hubbard satellites due to local charge excitations on the impurity, and a central low-energy Kondo resonance. We denote the half-width at half-maximum of the $h = 0$ Kondo resonance by ω_K : the low-energy Kondo scale, proportional to the Kondo temperature T_K .

In both cases, increasing the applied field causes spectral weight to be redistributed from the lower to the upper Hubbard satellite, corresponding to the destabilization of \downarrow -spin electrons on the dot. The striking difference between the two is that for the 2LM (main figure), a significant redistribution occurs upon introducing an infinitesimal field (e.g., $h/\omega_K^{S=1} = 1 \times 10^{-6}$), whereas for the AIM this occurs only when $h/\omega_K \sim O(1)$ (inset). This reflects directly the behavior of the magnetization in Fig. 2 [see Eq. (18)]: the free spin associated with the USC FP is fully polarized by an infinitesimal field, while a finite $h \sim \omega_K$ is required to disrupt the Kondo singlet associated with the SC FP of the AIM.

The above high-frequency behavior is relatively straightforward compared to that at lower energies $\omega \sim \omega_K$, as now addressed, beginning with the AIM. The low-frequency behavior of the AIM spectrum in a magnetic field has received significant attention using various techniques,^{34–42} yet there is still some disagreement in the literature. Here we present results from accurate NRG calculations, with the aim of clarifying the issue.

At zero field, the Kondo resonance at p-h symmetry is centered on $\omega = 0$, symmetric to reflection about $\omega = 0$, and satisfies the Fermi liquid pinning condition $\pi \Gamma D_{11;\sigma}(\omega = 0) = 1$. Introduction of a finite h is well known to shift the resonance in $D_{11;\sigma}(\omega; h)$ away from $\omega = 0$ and diminish its height.³⁴ We define Δ_σ as the magnitude of this shift, as shown in the inset of Fig. 6.

The spin-summed spectrum $D_{11}(\omega; h)$ [= $\frac{1}{2} \sum_\sigma D_{11;\sigma}(\omega; h)$] is distinct from the individual $D_{11;\sigma}(\omega; h)$,

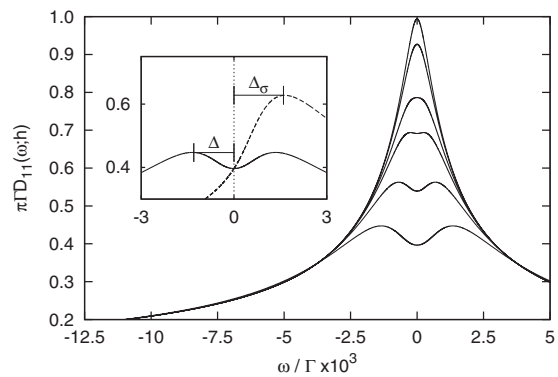


FIG. 6. Kondo resonance splitting in the spin-summed $D_{11}(\omega; h)$ for the AIM, on application of a magnetic field. $\tilde{U} = 20$, $\tilde{\epsilon} = -10$, and (top to bottom) $h/h_C = 0, 1/2, 1, 4/3, 2$, and 3 with $h_C = 0.27\omega_K$ and $\omega_K/\Gamma = 1.7 \times 10^{-3}$. Inset: Kondo peaks in $D_{11;\uparrow}(\omega; h)$ (solid) and $D_{11;\downarrow}(\omega; h)$ (dashed).

since the $\sigma = \uparrow$ and \downarrow Kondo resonances are shifted in opposite directions by the field. At sufficiently high fields, the two resonances are far apart and $D_{11}(\omega)$ contains two peaks separated by 2Δ (see Fig. 6, inset). As h is reduced, these peaks approach each other and are known³⁴ to coalesce at a field we denote h_C (Fig. 6, main). Our FDM-NRG calculations yield a universal value $h_C \simeq 0.27\omega_K$ in the Kondo regime ($U/\Gamma \gg 1$). In terms of the quasiparticle weight $Z = [1 - \partial \Sigma_{11}(\omega = 0)/\partial \omega]^{-1}$, easily extracted from FDM-NRG results for the dot self-energy $\Sigma_{11}(\omega)$, we obtain $h_C \simeq 0.40Z\Gamma$. This is in good agreement with the exact result of Ref. 46, $h_C/Z\Gamma = 0.39 \dots$

We have performed accurate NRG calculations to determine the universal scaling behavior of Δ_σ/h and Δ/h as a function of h/ω_K . Before discussing these results, it is worth explaining the calculational procedure itself. We find that to calculate Δ_σ and Δ accurately over a wide range of h/ω_K , it is necessary to combine results from different values of \tilde{U} . For a given \tilde{U} , one cannot obtain universal results for arbitrarily high h/ω_K , because universality arises only when h is much smaller than the nonuniversal scales Γ and U . Since ω_K is small but finite for a given \tilde{U} , there will always be a (large) h/ω_K at which h itself becomes comparable to the nonuniversal scales and the results then deviate from universality.

Since ω_K decreases exponentially with increasing \tilde{U} , this might suggest working with a very large \tilde{U} , for then one can reach very high values of h/ω_K before h itself becomes nonuniversal. However this is subject to a second problem, at the opposite end of the field scale. The energies that enter the Hamiltonian involve combinations of h , U , and Γ , and the double-precision arithmetic used in NRG thus places a lower limit on the size of h relative to U and Γ . If ω_K is too small, then low values of h/ω_K shift the dot energy levels by so little that they cannot be accurately represented in double precision.

As such, for a given \tilde{U} there is a range of fields encompassing in practice around four to five orders of magnitude, over which the universal scaling curve can be determined by the NRG. By combining results for different values of \tilde{U} , the full scaling curve can then be built up, and by choosing \tilde{U} 's such that the calculations overlap, one can obtain a measure of the accuracy of the calculation.

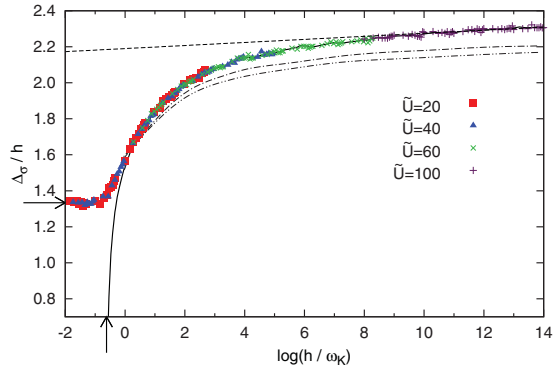


FIG. 7. (Color online) Universality in the field dependence of the spectral maximum, $\Delta_\sigma(h)$, in $D_{11;\sigma}(\omega; h)$ for the symmetric AIM. See text for discussion. Horizontal arrow indicates the exact low-field asymptote $\Delta_\sigma/h = 4/3$. Dashed line shows the high-field form $a \log(h/\omega_K) + c$. Solid line shows $\Delta(h)$, the position of the maxima in the spin-summed $D_{11}(\omega; h)$; the vertical arrow indicates the exact h_c .

The points in Fig. 7 show the resultant $\Delta_\sigma(h)/h$ obtained from a series of NRG calculations for $\tilde{U} = 20, 40, 60$, and 100. Results for different values of \tilde{U} indeed overlap when plotted versus h/ω_K , indicating universal scaling behavior. At low field $\Delta_\sigma/h \rightarrow 4/3$ as $h \rightarrow 0$, recovering the exact result from Fermi liquid theory.^{37,60} The splitting Δ_σ/h increases with h/ω_K , undergoing a rapid crossover around $h/\omega_K \sim 1$ and tending asymptotically to the limiting form $\Delta_\sigma/h \sim a \log(h/\omega_K) + c$, which behavior agrees with results obtained from the local moment approach.³⁷

We believe the low- h/ω_K behavior of the points in Fig. 7 to be numerically exact, having repeated our calculations significantly more accurately and obtained the same results. The numerics also agree with recent NRG calculations⁴² performed in the narrow region $-0.9 \lesssim \log(h/\omega_K) \lesssim 0.6$. As the field (and hence location of the spectral maximum) increases further, however, it becomes progressively more difficult to obtain accurate NRG results for Δ_σ . This is a direct consequence of the broadening procedure employed to obtain NRG spectra: broadening is necessarily performed on a logarithmic scale due to the inherent logarithmic discretization of the technique, so sharp spectral features at finite frequencies become increasingly difficult to resolve as they move away from $\omega = 0$. The problem can be resolved to some extent by using z -averaging⁵¹ and calculating the self-energy directly,⁵² but presently available computing power limits the extent to which this approach can be pushed. In Fig. 7, the points were obtained by averaging results from 10 z 's, with a broadening parameter³² $b = 0.1$. Increasing the number of z 's to 20 and working with $b = 0.07$ and 0.05 gives the dot-dashed and dot-dot-dashed lines in Fig. 7. The results are clearly sensitive to the broadening at high fields, although in each case they show qualitatively similar high-field behavior.

Figure 8 (right) shows analogous results for the spectral shift in $D_{ee;\sigma}(\omega; h)$ for the two-level model at p-h symmetry. Here we find the results to be even more sensitive to the NRG broadening procedure. The points show the splitting obtained from averaging 10 z 's with $b = 0.7$ (using four different bare values of U/Γ as before), while the short-dashed, long-dashed,

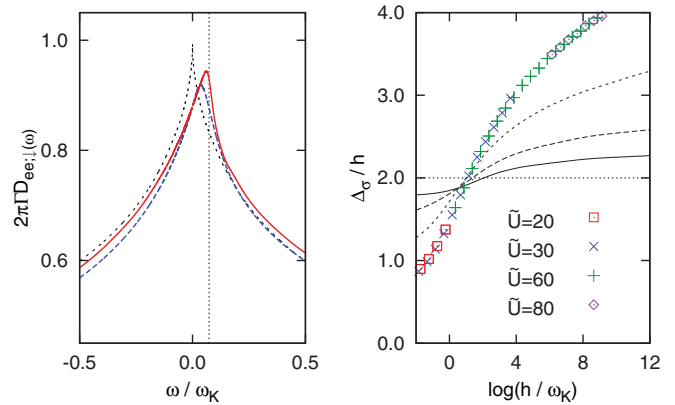


FIG. 8. (Color online) Field-induced shift of the underscreened Kondo resonance in the p-h-symmetric 2LM model. Left panel: the spectrum $D_{ee;\downarrow}(\omega)$ for $h = 0$ (short dashed line), and for $h/\omega_K^{S=1} = 0.366$ with two different broadening parameters: $b = 0.7$ (dashed line) and $b = 0.2$ (solid line). Right panel: Δ_σ/h as a function of $h/\omega_K^{S=1}$ for $b = 0.7$ (points), $b = 0.4$ (short-dashed), $b = 0.2$ (long-dashed), and $b = 0.1$ (solid), as discussed in the text. The results appear to be converging to $\Delta_\sigma/h = 2$ for all $h/\omega_K^{S=1}$; this limit is marked as a vertical dotted line in the left panel for the case $h/\omega_K^{S=1} = 0.366$.

and solid lines are from 20 z 's with $b = 0.4, 0.2$, and 0.1 , respectively. As the accuracy of the calculation increases, the splitting appears to be approaching $\Delta_\sigma/h = 2$ for all h , in marked contrast to the behavior of the AIM in Fig. 7.

To pursue this further, the left-hand panel of Fig. 8 shows $D_{ee;\downarrow}(\omega; h)$ for a representative low-field case, $h/\omega_K^{S=1} \simeq 0.0366$: the long-dashed line shows the spectrum obtained with broadening $b = 0.7$, while the solid line shows the $b = 0.2$ result. The figure clearly illustrates the sensitivity of the finite- h spectrum to the value of b employed, and in line with our conjecture above it appears that in the limit $b \rightarrow 0$ the peak position would lie at $2h$ (marked as a vertical dotted line in the figure).

The short-dashed line in Fig. 8 shows also the corresponding $h = 0$ spectrum for comparison, the form of which (including its zero-frequency cusp) has been discussed previously.^{24,61} It is reasonable to conjecture that the finite- h spectrum has a qualitatively similar form but shifted so that the cusp occurs at $\omega = 2h$, although at present it is not possible to confirm or refute this using currently feasible NRG calculations.

We conclude here with a point pursued further in Sec. V. Our discussion has concerned purely the following question: how does the *equilibrium spectrum* evolve with magnetic field in single- and two-level dots? Here we have deliberately not related the equilibrium spectrum to the finite-bias conductance, because Eq. (10) is approximate and (as shown explicitly later in relation to recent experiments) can give quantitatively wrong results for field strengths in excess of a few Kondo scales.³⁸ The figures shown here should *not*, therefore, be translated naively into quantitative predictions of conductance splittings. The only predictions for experiment that can currently be made with real certainty are those involving the zero-bias conductance. These are now discussed.

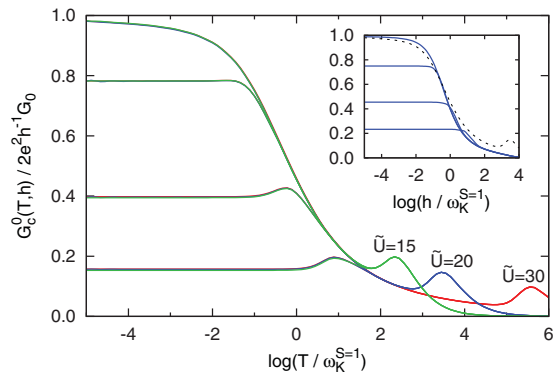


FIG. 9. (Color online) Scaling of zero-bias conductance for the 2LM at finite temperature and field. Top to bottom: $h/\omega_K^{S=1} = 0, 0.1, 1, \text{ and } 10$. $U = 2U' = 4J$ with $\tilde{U} = 30, 20, \text{ and } 15$ (red, blue, and green) corresponding to $\omega_K/\Gamma = 2.06 \times 10^{-5}, 1.64 \times 10^{-3}, \text{ and } 1.47 \times 10^{-2}$. Inset: $G_c^0(T, h)$ vs $h/\omega_K^{S=1}$ for $\tilde{U} = 20$ and $T/\omega_K^{S=1} = 0, 0.1, 1, 10$. $G_c^0(T, h = 0)$ vs $T/\omega_K^{S=1}$ (dashed), as in the main figure, is shown for comparison.

C. Zero-bias conductance

Figure 9 illustrates universality in the zero-bias conductance for the 2LM, as functions of $h/\omega_K^{S=1}$ and $T/\omega_K^{S=1}$. For specificity, we consider the p-h symmetric point $(x, y) = (0, 0)$ (which applies also to points along the line $y = -x$ deep in the USC phase, see Sec. III). The interactions are set at $U = 2U' = 4J_H$, and different values of $\tilde{U} = U/\Gamma$ are considered. For fixed $h/\omega_K^{S=1}$ (the values 0, 0.1, 1, and 10 are shown explicitly in Fig. 9), the zero-bias conductance $G_c^0(T, h)$ is seen to be universal in $T/\omega_K^{S=1}$, as is evident from clear scaling collapse of the different \tilde{U} curves. Scaling naturally breaks down at nonuniversal scales $T \sim \min(\Gamma, U)$, and for $T \sim U$ the curves show peaks associated with incoherent sequential tunneling.

Notice that at finite temperature for a given, sufficiently large $h/\omega_K^{S=1}$ (in excess of ~ 0.1 in Fig. 9) there is a universal peak in the zero-bias conductance at a temperature $T \sim h$. This is analogous to the peak at finite frequency in the $T = 0$ equilibrium spectrum, Sec. IV B. Yet here the peak exists in a quantity that is both directly measurable by experiment and calculable exactly by theory. Until theory is able to capture accurately the nonequilibrium conductance as a function of source-drain bias, we suggest that the field dependence of *this* peak in the *zero-bias* conductance, and more generally the h and T dependence of G_c^0 , be touchstones by which the universality of experiment is assessed.

The inset to Fig. 9 shows another way of viewing the universal conductance curves. Here we fix $T/\omega_K^{S=1}$ (at values 0, 0.1, 1, and 10, top to bottom) and vary the magnetic field $h/\omega_K^{S=1}$ over many orders of magnitude. Notice that there is no incoherent peak at large h , in contrast to that in the T dependence for fixed h . This is because at large fields the dot is completely spin-polarized, and its conductance is thus weak.

Before moving to particular experiments, we consider specifically the $T = 0$ zero-bias conductance. For $h = 0$, this is related to the scattering phase shift, δ , via Eq. (9) and the relation $2\pi\Gamma D_{ee}(0) = \sin^2 \delta$. In previous work,²⁴ we derived

an exact Friedel-Luttinger sum rule

$$\delta = \frac{\pi}{2} n_{\text{imp}} + I_L \quad (19)$$

relating δ to the excess charge induced by the impurity, n_{imp} (equivalent to $\langle \hat{n}_1 + \hat{n}_2 \rangle$ in the infinite bandwidth limit), and the Luttinger integral I_L defined by

$$I_L = \text{Im Tr} \int_{-\infty}^0 d\omega \frac{\partial \Sigma(\omega)}{\partial \omega} \mathbf{G}(\omega). \quad (20)$$

We showed²⁴ that while $I_L = 0$ as usual for the screened Fermi liquid phase, $|I_L| = \pi/2$ is by contrast characteristic of the USC phase (*regardless* of the bare model parameters), reflecting the lack of adiabatic continuity of the USC phase to the noninteracting limit.

On applying a magnetic field, the analysis of Ref. 24 readily generalizes to the case of broken spin symmetry. Now one has $2\pi\Gamma D_{ee,\sigma}(0; h) = \sin^2 \delta_\sigma$, with separate phase shifts for $\sigma = \uparrow, \downarrow$ of the form

$$\delta_\sigma = \pi n_{\text{imp},\sigma} + I_{L\sigma}, \quad (21)$$

where

$$I_{L\sigma} = \text{Im Tr} \int_{-\infty}^0 d\omega \frac{\partial \Sigma_\sigma(\omega)}{\partial \omega} \mathbf{G}_\sigma(\omega), \quad (22)$$

and such that¹⁹ [via Eq. (9)]

$$\frac{G_c^0(T=0)}{(2e^2/h)G_0} = \frac{1}{2} [\sin^2 \delta_\uparrow + \sin^2 \delta_\downarrow]. \quad (23)$$

As mentioned in Sec. IV A, the USC fixed point is unstable for any $h > 0$, which means that all NRG flows terminate at the SC fixed point. Since the SC fixed point is characteristic of adiabatic continuity to the noninteracting limit, for any finite h one would expect the two Luttinger integrals $I_{L\sigma}$ to vanish. This we have indeed confirmed by direct numerical calculation.

The Luttinger integrals thus change *discontinuously* on introducing an arbitrarily small magnetic field at any point within the USC phase. One naturally then wonders whether this has consequences for the conductance. To answer this, one can write the phase shifts in terms of the excess charge and magnetization¹⁹ defined by

$$\begin{aligned} n &= n_{\text{imp},\uparrow} + n_{\text{imp},\downarrow}, \\ m &= n_{\text{imp},\uparrow} - n_{\text{imp},\downarrow} \end{aligned} \quad (24)$$

(with $n \equiv \langle \hat{n}_1 + \hat{n}_2 \rangle$ and $m \equiv m_1 + m_2$ in the infinite bandwidth limit), from which Eqs. (21) and (23) give

$$\frac{G_c^0(T=0)}{(2e^2/h)G_0} = \frac{1}{2} \{1 - \cos[\pi n(h)] \cos[\pi m(h)]\} \quad (25)$$

for *any* point in the (x, y) plane when $h > 0$. But at points corresponding to the USC phase at zero field, $m(h=0^+) = 1$ (see, e.g., Fig. 3), i.e., it too jumps discontinuously on introducing an infinitesimal field. Substituting this into Eq. (25) gives

$$\frac{G_c^0(T=0)}{(2e^2/h)G_0} = \cos^2 \left(\frac{\pi n}{2} \right) \quad (h = 0^+), \quad (26)$$

which is precisely the conductance obtained²⁴ in the USC phase for $h = 0$. In other words, although both the Luttinger integrals and magnetization change discontinuously in the USC phase on applying a field—and hence the cases $h = 0$ and $h = 0^+$ are different—the conductance itself contains no signature of these abrupt changes.

V. EXPERIMENTAL RESULTS

A. Semiconductor quantum dots

Turning now to experiment, we begin by considering the work of Liu *et al.* in Ref. 44, where the magnetic field dependence of the spin- $\frac{1}{2}$ Kondo effect was measured in a GaAs device. In the experiment, the gates were adjusted to produce two different realizations of a quantum dot from the same device, referred to as configurations I and II, with different dot-lead tunnel barriers.⁴⁴

We adopt the simplest theoretical model of the device, the single AIM in Eq. (1), and parametrize it using experimental data.⁴⁴ At $T = 0$, the equilibrium model is characterized by the two dimensionless parameters⁶² U/Γ and ϵ_1/Γ , with the experimental $U = 1.4$ meV.⁴⁴ The level energy ϵ_1 is as usual taken to depend linearly on the applied gate voltage V_g : we write $\epsilon_1 + U/2 = \alpha e \delta V_g$, with δV_g the difference between the experimental gate voltage and its value in the center of the Coulomb blockade valley, and α is a dimensionless constant. Finally, comparison to experimental splittings at finite bias requires the dimensionless quantity λ (Sec. II), which controls the partitioning of the source-drain bias V_{sd} between the leads.

The values of U/Γ and α appropriate to experiment could in principle be obtained by comparing experimental and theoretical curves for T_K/T_K^0 versus $\epsilon_1 + U/2$ over a sufficiently wide δV_G range, where T_K^0 is the Kondo scale at the center of the Coulomb valley (i.e., $\epsilon_1 + U/2 = 0$). We find, however, that the range of available data in Ref. 44 is insufficient to determine U/Γ reliably in this way, since near the middle of the Coulomb valley where the experimental results have been obtained, the functional form of the theoretical Kondo scale depends only on the ratio $\alpha^2 U/\Gamma$, and hence U/Γ and α cannot be obtained separately. We have therefore used both the zero- and finite-field behavior to parametrize the model, choosing the best values of U/Γ , α , and λ to agree with the available experimental data. After analyzing a wide range of parameter space, we obtain the values shown in Table I.

Before showing our NRG results, we comment further on the origin of these parameters. The values of U/Γ and λ were determined first, simply by optimal fitting to the finite-field data at the center of the Coulomb blockade valley (shown in Fig. 10), using the approximate Eq. (10). Then to obtain α , we compared the experimental T_K/T_K^0 versus gate voltage to

TABLE I. Parameters obtained for the two dot configurations of Ref. 44, by comparison to NRG results.

Configuration	U/Γ	α	λ	\tilde{T}_K^0 (K)
I	8.0	0.020	0.7	0.2
II	7.2	0.017	0.65	0.3

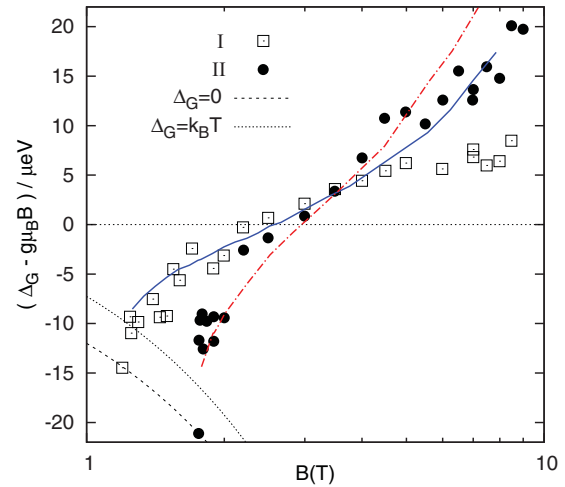


FIG. 10. (Color online) Splitting of the Kondo conductance peak on application of a magnetic field, at the center of the Coulomb blockade valley ($\epsilon_1 = -U/2$). The open squares and filled circles are experimental data,⁴⁴ while the blue (solid) and red (dot-dashed) lines are NRG calculations for $U/\Gamma = 8$, $\lambda = 0.7$ and $U/\Gamma = 7.2$, $\lambda = 0.65$, respectively. The dashed line is $\Delta_G = 0$ and the dotted line is $\Delta_G = k_B T$ with the experimental $T = 55$ mK.

our corresponding theoretical results, themselves taken from explicit NRG calculations. We observe that the values of α so obtained are in line with the experimental estimate⁴⁴ $\alpha \simeq 0.024$. Noting that the quantity denoted “ Γ ” in Ref. 44 is 2Γ here, the ratios of U/Γ determined therein are 5.3 and 4.0 for configurations I and II, respectively. Our values are a little larger than these, contributory factors being (a) that in determining Γ from the widths of the charging peaks one must bear in mind their many-body broadening,^{63,64} which typically gives them a half-width at half maximum of around $1.5 - 2\Gamma$ (rather than Γ , as arises in the noninteracting limit), and (b) fitting Kondo scales to the Haldane formula used in Ref. 44 underestimates U/Γ , since it applies asymptotically in the limit $U/\Gamma \gg 1$. Given the U/Γ , and the experimental $U = 1.4$ meV,⁴⁴ we then calculate the Kondo temperatures \tilde{T}_K^0 as shown in Table I, with \tilde{T}_K^0 defined (as in experiment⁴⁴) such that $G_c^0(\tilde{T}_K^0, 0)/G_0 = e^2/h$ at $\epsilon_1 = -U/2$. Given the sensitivity of absolute Kondo scales to the bare model parameters, our values are in good agreement with the experimental estimates of 0.3 and 0.63 K (configurations I and II, respectively).⁴⁴

To add further support to these parameters, we note that a consistent, independent determination of λ can be obtained from the experimental conductance map, Fig. 1(a) of Ref. 44. The slopes of the diagonal sequential tunneling peaks, when plotted with V_{sd} as the horizontal axis, are readily shown⁶⁵ to be proportional to $1/\lambda$ and $1/(1 - \lambda)$, and hence their ratio yields $\lambda/(1 - \lambda)$. From the experimental data,⁴⁴ we extract $\lambda \approx 0.7$, in agreement with our values listed above.

With the parameters thus chosen, Fig. 10 compares the size of the peak splittings Δ_G (defined as half the peak to peak splitting in the finite-bias conductance, using the notation of Ref. 44) from theory—using the approximate Eq. (10)—and experiment,⁴⁴ both obtained in the center of the Coulomb valley ($\epsilon_1 = -U/2$). We have plotted the data in the form employed in Ref. 44, subtracting the Zeeman splitting

$g\mu_B B = 2h$ from the actual splitting Δ_G to emphasize the deviation of the two. The open squares and filled circles are the experimental data for dots I and II, respectively (as in Fig. 4 of Ref. 44), while the blue (solid) and red (dot-dashed) lines are the corresponding theoretical results. The latter have been obtained at $T = 0$: we note that the experimental splittings are generally somewhat in excess of T (see the dotted line in Fig. 10), and hence temperature does not play an important role in the analysis. Note also that for fields very close to the coalescence point where Δ_G vanishes (i.e., when the splittings approach the dashed curve in Fig. 10), it is difficult to extract the precise value of the splitting, and hence we show only the sections of the curves for which the splitting can be determined reliably.

The agreement between theory and experiment is very good. In both cases, theory reproduces well the low-field splittings, and the curves track the experimental results up to fields of around 5 T, corresponding to Kondo peak splittings of around $1-2T_K^0$. At higher fields, the theoretical curves certainly deviate from experiment, which we take to be a sign of the breakdown of the quasiequilibrium approximation in Eq. (10). Recently, Schmitt and Anders have extended their nonequilibrium scattering-states NRG approach to the Anderson model in a magnetic field.⁴⁵ This approach offers a promising means of determining peak splittings out of equilibrium, and further work comparing its predictions with those of Eq. (10) should help to establish the regimes of the model where nonequilibrium effects play a large role. One interesting question to be pursued here is the effect of left-right asymmetry in the coupling to the leads,⁴⁵ since within the quasiequilibrium approximation this affects only the dimensionless G_0 in Eq. (10) and thus simply rescales the conductance uniformly.

The final point to note here is that theory reproduces the crossing of the two curves identified in the experiment. We find this to be entirely a consequence of the slightly different λ 's for dots I and II: if one repeats the calculations with equal λ 's, the curves do not cross. This, in fact, is a special case of a more general finding: for a given λ , our calculations show that curves with different U/Γ never cross (even if one or both curves correspond to nonuniversal parameter regimes). Hence the crossing of the two curves should not be taken⁴⁴ to indicate the breakdown of universal scaling *per se*.

B. Carbon nanotube quantum dots

We now turn to an analysis of the experiments of Quay *et al.*,⁴³ in which the magnetic field dependences of both spin- $\frac{1}{2}$ and spin-1 Kondo effects were measured in different Coulomb valleys of a carbon nanotube device.

1. Spin- $\frac{1}{2}$ Kondo valley

In the spin- $\frac{1}{2}$ valley, conductance maps were obtained⁴³ at zero and finite B as a function of gate and source-drain biases, and the evolution of the finite-bias conductance was also measured as a function of B . The splitting of the Kondo resonance at finite bias was compared to various theoretical predictions in the literature, the level of agreement being rather poor.⁴³ In this section, we explain why the experiment did not

recover the expected behavior. First, we again parametrize the model from zero-field experimental data.

As before, the spin- $\frac{1}{2}$ Kondo effect in experiment is captured well by the Anderson impurity model, Eq. (1). By comparing to the experimental conductance maps in Ref. 43, we find the value $U/\Gamma = 8.5$ gives optimal agreement with the experimental data at both zero and finite fields. The value of $\lambda \simeq 0.58$ can separately be extracted as described in the previous section,⁶⁵ and the experimental U can be determined from the Coulomb peak position in Fig. 2(d) of Ref. 43: it is readily seen to be approximately 2 meV, and hence $\Gamma \simeq 0.24$ meV. From NRG calculations at $T = 0$, we then find $\tilde{T}_K^0 = 0.094\Gamma \simeq 0.022$ meV $\simeq 0.25$ K, lower than the experimentally estimated value of 2 K. This means that the temperature of the device ($T = 352$ mK)⁴³ is then on the order of the Kondo scale, rather than being somewhat less than it. We believe this to be more consistent with experiment, as is now explained.

The magnitude of the experimental Kondo scale can be gauged by inspection of Fig. 2(d) of Ref. 43. If these results were obtained at a temperature somewhat below \tilde{T}_K^0 , the Kondo resonance would hardly be eroded by temperature, and instead one would naturally attribute the diminution of the zero-bias conductance from the unitarity limit of $2e^2/h$ to the asymmetry of the left and right dot-lead couplings (manifest in a $G_0 \approx 0.4$). But it is then difficult to explain the heights of the Kondo resonance *relative* to that of the Coulomb peaks since [with the caveat that Eq. (10) is approximate] we would expect⁶³ the latter to be around a quarter of the height of the former for $T \ll \tilde{T}_K^0$. We believe it much more likely that \tilde{T}_K^0 is closer to the temperature of the device, eroding more the Kondo resonance and thus reducing its height to something closer to that of the Coulomb peaks.

Moving on to our conductance results, Fig. 11(a) shows the theoretical conductance map, calculated from Eq. (10), to be compared to Fig. 2(a) of Ref. 43. The general agreement is good; the theory reproduces the intense sequential tunneling peaks when the dot level is resonant with one of the lead chemical potentials, the somewhat weaker Coulomb diamond, and the narrower Kondo resonance at zero bias near the center of the Coulomb blockade valley. Figure 11(b) shows the effect of switching on a magnetic field $h/\Gamma = 0.5$: again, the qualitative agreement with experiment is very good, including now a clear “ellipsoidal” ring around the center of the Coulomb blockade valley resulting from the splitting of the Kondo resonance by the field.

The field dependence is shown in more detail in Figs. 11(c) and 11(d), which both show the field dependence of the conductance in the center of the Coulomb blockade valley. We again recover the key features of the experiment [Figs. 2(c) and 2(d) of Ref. 43]. For fields sufficiently small compared to the zero-field Kondo scale ($h/\Gamma \lesssim 0.2$), the Kondo resonance remains intact, while for larger fields it is progressively split and ultimately destroyed with increasing h , eventually leading to a region of almost zero conductance around zero bias. Comparing the slices through the data in Fig. 11(d) to those of the experiment, we again observe good qualitative agreement between the two.

We should point out at this stage that the value of $h/\Gamma = 0.5$ chosen in Fig. 11(b) corresponds, in physical units, to a field

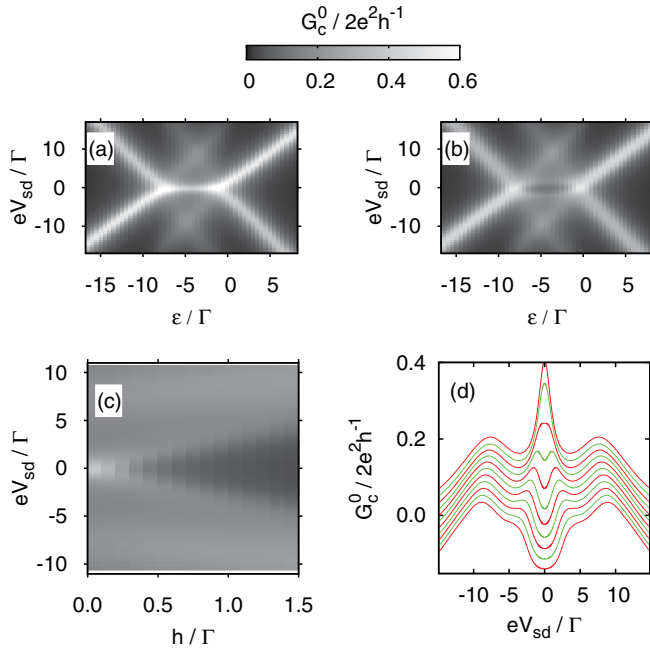


FIG. 11. (Color online) Spin- $\frac{1}{2}$ conductance maps at zero and finite magnetic field: to compare with Fig. 2 of Ref. 43. An AIM is used with $\tilde{U} = 8.5$ (giving $\omega_K/\Gamma \simeq 0.15$), with $T = \omega_K$ and $G_0 = 1$. (a) Zero-field conductance: a clear Kondo ridge is seen at zero bias voltage. (b) A finite field, $\tilde{h} = 0.5$, splits this ridge into twin peaks away from zero bias. (c) Evolution of the Kondo peaks with field at the middle of the Coulomb valley (p-h symmetry). (d) Vertical slices through (c) with (top to bottom) $\tilde{h} = 0, 0.1, 0.2, \dots, 0.9$, offset by $0.02 \cdot 2e^2 h^{-1}$ per slice.

of about 2 T, around half the experimental field. This again we attribute primarily to the breakdown of the quasiequilibrium approximation Eq. (10) at fields larger than a couple of T_K : as seen earlier in Fig. 10, the approximation tends to overestimate the splitting at these high fields, and hence a smaller h/Γ must be used in the calculation to obtain the same absolute splitting as the experiment. Based on the comparison of the previous section, noting the theoretical value here of $\tilde{T}_K^0 = 0.094\Gamma$, we would estimate that the quasiequilibrium approximation begins to break down for this experiment at fields $B \gtrsim 1$ T.

While the latter means we cannot compare quantitatively our NRG predictions at finite field to those of the experiment over the whole range of fields measured, we nonetheless believe the parametrization of the experiment to be reliable at low magnetic fields. This allows us to make order-of-magnitude predictions that explain the significance of the experimental results and the reason for the apparent disagreement with theory,⁴³ as is now explained.

To summarize the analysis of Ref. 43, first the splitting of the Kondo peak with field was extracted from the experimental data and plotted versus B . It was found that half the splitting tends to the form $\delta = g\mu_B B$ at high field (with $g \simeq 2.07$). Direct comparison was then made between the full field dependence of the splitting obtained from several theories, and experiment.

We point out that there are two basic problems with making this comparison. First and foremost, if one is interested in the *universal* form of the Kondo splitting, the experimental

parameters need to satisfy both $U/\Gamma \gg 1$ and $h \ll \min(\Gamma, U)$. The former condition is necessary to ensure that the experiment is well-described by an effective Kondo model at low energies, and arises because the Schrieffer-Wolff transformation that maps the full Anderson model onto the Kondo model is formally valid in the asymptotic limit $U/\Gamma \gg 1$. The latter condition defines what is meant here by “low energies”: even if U/Γ is large, the effective Kondo description will always break down at energies of the order of the nonuniversal scale Γ , and the results on such an energy scale will simply not show universal Kondo form.

One could argue that the $U/\Gamma \simeq 8.5$ here is sufficiently large for the experiment to be well described by a Kondo model at zero field, although we believe this to be a somewhat more borderline case. The main problem, however, is that the experimental U and Γ are too small for the high-field results to be universal. This can in fact be seen directly from Fig. 2(d) of Ref. 43 [see also Figs. 11(b) and 11(d)]: even at moderate fields of 2–3 T, the Kondo (“Zeeman”) peaks are already overlapping significantly the nonuniversal Coulomb peaks. More formally, to be universal for some given h/T_K requires $h/\Gamma \ll 1$, the experimental $U = 2$ meV,⁴³ and $\Gamma \simeq 0.2$ meV as above, from which $g\mu_B B \ll \Gamma$ when $B \ll 2$ T.

The second problem is that the predictions for the theoretical conductance^{34,36,37} have all been made using (either explicitly or implicitly) the approximation of Eq. (10), rather than from a full-blown nonequilibrium approach. Even when we use the appropriate nonuniversal parameters in our NRG calculations, the comparison to both the present experiment and that of the previous section suggests that Eq. (10) is quantitatively reliable only for fields smaller than a few Kondo scales,³⁸ and even then is strongly dependent on the value of λ . Until nonequilibrium approaches such as the scattering-states NRG⁴⁵ become more feasible, the quantitative, universal form of the conductance splitting for $h \gg \tilde{T}_K^0$ is an open question; one should certainly not expect *a priori* to obtain quantitative agreement between experiment and Eq. (10).

2. Spin-1 Kondo valley

Finally, we consider the effect of magnetic field on the conductance of the two-level model, Eq. (2), to make a comparison with the spin-1 Kondo valley experiments of Ref. 43. Since there are more interactions in the two-level Hamiltonian than the AIM, it is obviously harder to parametrize the model from the available data in a fully systematic manner. We have thus endeavored to choose physically reasonable parameter values that reproduce qualitatively the experimental results (cf. those used for the experimental comparison of Ref. 24), from which we find $U/\Gamma = 12$, $U'/\Gamma = 6$, $J_H/\Gamma = -0.5$, and $(\epsilon_2 - \epsilon_1)/\Gamma \equiv \Delta\epsilon/\Gamma = 4.5$. For simplicity, we take $T = 0$, $\lambda = \frac{1}{2}$, and $G_0 = 1$. Choosing a reasonable value of $\Gamma \sim 0.25$ meV gives, e.g., a charging energy $U \sim 3$ meV and level spacing $\Delta\epsilon \sim 1$ meV, both of which are within typical experimental estimates.

Figure 12(a) shows the resultant splitting of the “underscreened Kondo” conductance peak at a point in the USC phase near the zero-field USC/SC phase transition [as indicated by the tail of the arrow in the phase diagram Fig. 12(c)]. The figure is qualitatively similar to that for the spin- $\frac{1}{2}$ Kondo peak

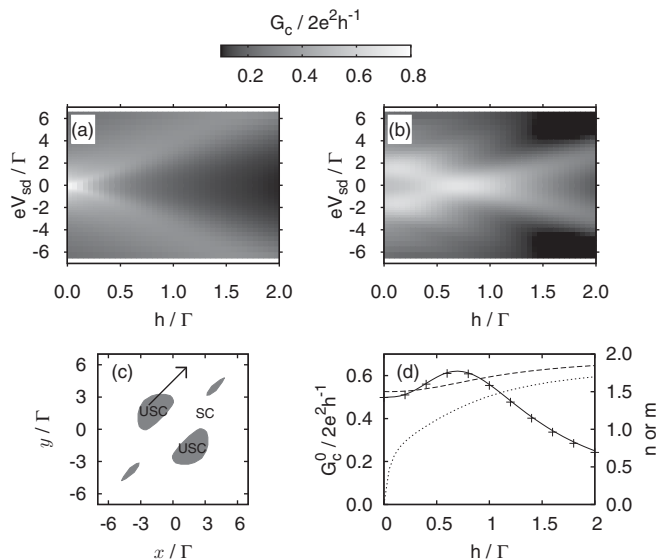


FIG. 12. Conductance maps for the 2LM close to the $h = 0$ phase transition, for $\tilde{U} = 12$, $\tilde{U}' = 6$, $\tilde{J}_H = -0.5$, and $\Delta\tilde{\epsilon} = 4.5$. To be compared to Figs. 5(a) and 5(b) of Ref. 43. (a) USC phase for $y = -x = 2.25\Gamma$ ($x = \epsilon_1 + \frac{1}{2}U + U'$ and $y = x + \Delta\epsilon$, with $\epsilon_1 \propto V_{\text{gate}}$). The conductance peak splits on applying a field. (b) SC phase for $(x, y) = (1.25\Gamma, 5.75\Gamma)$. The $h = 0$ Kondo antiresonance is “filled in” for $h > 0$; full discussion in text. (c) $h = 0$ phase diagram for the above parameters as a function of x/Γ and y/Γ , with the arrow showing the “trajectory” taken in going from (a) to (b). (d) Zero-bias cut through (b) (crosses), along with the total dot occupation number $n(h)$ (dashed), magnetization $m(h)$ (dotted), and $G_c^0/(2e^2/h)$ as given by Eq. (25) (solid).

in a magnetic field [Fig. 11(c)] but, as noted in the case of a stretched spin-1 molecule,²⁸ the field at which the zero-bias peak is destroyed is a somewhat smaller fraction of the Kondo scale. This naturally reflects the sharper USC Kondo resonance (see Fig. 8, left) compared to the spin- $\frac{1}{2}$ Kondo case.

The Kondo scale $\omega_K^{S=1}$ for the chosen parameters is $\omega_K^{S=1} \simeq 0.66\Gamma \simeq 0.2 \text{ meV} \simeq 2 \text{ K}$, which again appears roughly in line with the widths of the Kondo peaks in the experimental conductance maps.⁴³ This means it is perhaps misleading to refer to the basic phenomenology here as “underscreened Kondo” physics, since resonance widths on the order of Γ imply the model is far from being well described by an effective spin-1 Kondo model *per se*. As for the semiconducting quantum dot analyzed previously,²⁴ it also appears that the experimental trajectory as a function of gate voltage ($\epsilon_1 \propto V_{\text{gate}}$) just cuts the “edge” of the USC phase where the USC-phase Kondo scale is relatively high.

Just across the phase boundary into the SC Fermi liquid phase, we obtain the conductance map shown in Fig. 12(b). Here we have kept the interactions and $\Delta\epsilon$ fixed, but increased ϵ_1 by 3.5Γ from its value in Fig. 12(a) [the head of the arrow in Fig. 12(c) gives the precise location relative to the phase boundary]. The qualitative agreement between theory and experiment [Fig. 5(b) of Ref. 43] is again very good. We recover all basic features seen in experiment:⁴³ at zero field, the conductance peaks at around $\pm 2\Gamma \simeq \pm 0.5 \text{ meV}$, reflecting at zero bias the *antiresonance* in the equilibrium spectrum just inside the SC phase.^{14,24} These peaks move toward each

other, cross, and ultimately move apart with increasing field, which can be loosely associated with a crossing of the isolated dot singlet and lowest triplet states, with a finite-field Kondo effect taking place at the crossing point (again, the “Kondo” scale here is rather large, and as such one cannot describe the low-energy behavior in terms of a pure spin- $\frac{1}{2}$ Kondo model). We note that in our calculations, the crossing takes place at $h \sim 0.7\Gamma \simeq 0.2 \text{ meV}$ and hence $B \sim 3 \text{ T}$, again in good agreement with experiment. One can also make out various weaker features in the conductance, parallel to the main features and again seen experimentally, which mirror transitions from the isolated dot singlet to the higher energy triplet states.⁴³

The zero-bias conductance is analyzed further in Fig. 12(d), which is a cut through Fig. 12(b) at $eV_{\text{sd}} = 0$ [crosses are the NRG data from Fig. 12(b)]. With increasing field, $G_c^0/(2e^2/h)$ increases from its zero-field value of $\sim \frac{1}{2}$, passes through a maximum at $h/\Gamma \sim 0.7$ [as is evident from Fig. 12(b)], and decreases monotonically thereafter. Also shown are the total dot occupation $n(h)$ and magnetization $m(h)$ [see Eq. (24)], both of which increase smoothly and monotonically as the ground state evolves with increasing field. At zero field, the dot is in a mixed-valent regime, with $n(h=0) \simeq 1.5$ (and $m = 0$). But with increasing field, the dot ground state becomes progressively more like the simple $S_z = 1$ component of the isolated-dot triplet, with both total charge and magnetization tending to 2 for $h/\Gamma \gg 1$ (i.e., $n_{\text{imp},\uparrow} \simeq 2$, $n_{\text{imp},\downarrow} \simeq 0$).

While the zero-bias conductance shown above is calculated using Eq. (9), and as such probes single-particle spectra, its field dependence shown in Fig. 12(d) should equally be explicable from Eq. (25) (Sec. IV C), expressed solely in terms of the dot charge and magnetization. That this is indeed so is shown directly in Fig. 12(d): the solid line is calculated from Eq. (25), and seen to be in very good agreement with the direct NRG calculations.

VI. CONCLUDING REMARKS

In this paper, we have considered in some detail the effects of an applied magnetic field on single- and two-level quantum dots tunnel-coupled to a metallic lead, including magnetization, single-particle dynamics, and conductance, and highlighting for the two-level model in particular the rather subtle differences between the limits $h = 0$ and $h \rightarrow 0$. We have used NRG to analyze critically the field-dependent shift of the Kondo resonances in the two models, providing an algorithm that, in principle, can generate the universal scaling behavior over arbitrarily large h/ω_K ranges, limited in practice only by the logarithmic broadening inherent to NRG. For the single-level AIM, calculations can now be performed sufficiently accurately to achieve convergence up to fields of around $h \sim 100\omega_K$; for the two-level model, convergence is slower, but it appears to indicate a constant spectral shift $\Delta_\sigma = 2h$ for all fields in the universal regime.

We have also made a direct comparison between NRG calculations and two recent sets of conductance experiments on quantum dots in a magnetic field,^{43,44} using Anderson-type models for the dots to determine bare parameters corresponding to the experimental realizations. Agreement between

theory and experiment is found to be very good qualitatively (essentially all salient experimental features are captured by the models), and even quantitatively—see, e.g., Fig. 10—provided the system is not “too far out of equilibrium.” Since NRG provides in essence numerically exact results, the deviation of calculations from experiment provides a measure of the quantitative reliability of the quasiequilibrium approximation in Eq. (10), used throughout to calculate conductance; we find it typically breaks down when the field-induced splitting exceeds somewhat the zero-field Kondo scale.

We have argued that neither experiment^{43,44} considered has measured the *universal* conductance splitting of the spin- $\frac{1}{2}$ Kondo effect, and we have emphasized (Sec. V A) the considerable sensitivity of the field dependence of the conductance peak to the partitioning of the bias potential between the leads (embodied in λ)—over which, to our

knowledge, there is relatively little experimental control. In addition, as above, Eq. (10) for the conductance is approximate out of equilibrium, and until nonequilibrium approaches such as the scattering states NRG⁴⁵ are sufficiently developed to become the mainstay, the present theoretical tools are limited in that respect.

In view of the above, we suggest that more experimental attention should be given to the *equilibrium*, zero-bias conductance. Given exactly by Eq. (9), and independent of λ , its field dependence can be calculated exactly (see, e.g., Sec. IV C). We believe it presents a better prospect for ascertaining universality in the magnetic field dependence of spin- $\frac{1}{2}$ and spin-1 Kondo effects in real quantum dots.

ACKNOWLEDGMENT

We thank the EPSRC-UK for financial support.

-
- ¹A. C. Hewson, *The Kondo Problem to Heavy Fermions* (Cambridge University Press, Cambridge, 1993).
- ²L. P. Kouwenhoven *et al.*, in *Mesoscopic Electron Transport*, edited by L. L. Sohn (Kluwer, Dordrecht, 1997).
- ³W. G. van der Wiel, S. De Franceschi, J. M. Elzerman, T. Fujisawa, S. Tarucha, and L. P. Kouwenhoven, *Rev. Mod. Phys.* **75**, 1 (2003).
- ⁴M. Pustilnik and L. I. Glazman, *J. Phys. Condens. Matter* **16**, R513 (2004).
- ⁵S. Andergassen, V. Meden, H. Schoeller, J. Splettstoesser, and M. R. Wegewijs, *Nanotechnology* **21**, 272001 (2010).
- ⁶S. Ilani and P. L. McEuen, *Annu. Rev. Condens. Matter Phys.* **1**, 1 (2010).
- ⁷L. I. Glazman and M. E. Raikh, *Pisma Zh. Eksp. Teor. Fiz.* **47**, 378 (1988) [*JETP Lett.* **47**, 452 (1988)].
- ⁸T. K. Ng and P. A. Lee, *Phys. Rev. Lett.* **61**, 1768 (1988).
- ⁹Y. Meir and N. S. Wingreen, *Phys. Rev. Lett.* **68**, 2512 (1992).
- ¹⁰D. Goldhaber-Gordon, H. Shtrikman, D. Mahalu, D. Abusch-Magder, U. Meirav, and M. A. Kastner, *Nature (London)* **391**, 156 (1998).
- ¹¹S. M. Cronenwett, T. H. Oosterkamp, and L. P. Kouwenhoven, *Science* **281**, 540 (1998).
- ¹²M. Pustilnik and L. I. Glazman, *Phys. Rev. Lett.* **85**, 2993 (2000).
- ¹³K. Kikoin and Y. Avishai, *Phys. Rev. Lett.* **86**, 2090 (2001).
- ¹⁴W. Hofstetter and H. Schoeller, *Phys. Rev. Lett.* **88**, 016803 (2001).
- ¹⁵M. Pustilnik and L. I. Glazman, *Phys. Rev. Lett.* **87**, 216601 (2001).
- ¹⁶M. Vojta, R. Bulla, and W. Hofstetter, *Phys. Rev. B* **65**, 140405 (2002).
- ¹⁷M. Pustilnik, L. I. Glazman, and W. Hofstetter, *Phys. Rev. B* **68**, 161303 (2003).
- ¹⁸W. Hofstetter and G. Zarand, *Phys. Rev. B* **69**, 235301 (2004).
- ¹⁹M. Pustilnik and L. Borda, *Phys. Rev. B* **73**, 201301 (2006).
- ²⁰R. Zitko and J. Bonca, *Phys. Rev. B* **74**, 045312 (2006).
- ²¹R. Zitko and J. Bonca, *Phys. Rev. B* **76**, 241305 (2007).
- ²²A. Posazhennikova, B. Bayani, and P. Coleman, *Phys. Rev. B* **75**, 245329 (2007).
- ²³P. Roura Bas and A. A. Aligia, *Phys. Rev. B* **80**, 035308 (2009).
- ²⁴D. E. Logan, C. J. Wright, and M. R. Galpin, *Phys. Rev. B* **80**, 125117 (2009).
- ²⁵P. S. Cornaglia, P. Roura Bas, A. A. Aligia, and C. A. Balseiro, *Europhys. Lett.* **93**, 47005 (2011).
- ²⁶S. Florens, A. Freyn, N. Roch, W. Wernsdorfer, F. Balestro, P. Roura-Bas, and A. A. Aligia, *J. Phys. Condens. Matter* **23**, 243202 (2011).
- ²⁷A. Kogan, G. Granger, M. A. Kastner, D. Goldhaber-Gordon, and H. Shtrikman, *Phys. Rev. B* **67**, 113309 (2003).
- ²⁸N. Roch, S. Florens, T. A. Costi, W. Wernsdorfer, and F. Balestro, *Phys. Rev. Lett.* **103**, 197202 (2009).
- ²⁹J. J. Parks *et al.*, *Science* **328**, 1370 (2010).
- ³⁰K. G. Wilson, *Rev. Mod. Phys.* **47**, 773 (1975).
- ³¹H. R. Krishna-murthy, J. W. Wilkins, and K. G. Wilson, *Phys. Rev. B* **21**, 1003 (1980).
- ³²R. Bulla, T. A. Costi, and T. Pruschke, *Rev. Mod. Phys.* **80**, 395 (2008).
- ³³P. W. Anderson, *Phys. Rev.* **124**, 41 (1961).
- ³⁴T. A. Costi, *Phys. Rev. Lett.* **85**, 1504 (2000).
- ³⁵W. Hofstetter, *Phys. Rev. Lett.* **85**, 1508 (2000).
- ³⁶J. E. Moore and X.-G. Wen, *Phys. Rev. Lett.* **85**, 1722 (2000).
- ³⁷D. E. Logan and N. L. Dickens, *J. Phys. Condens. Matter* **13**, 9713 (2001).
- ³⁸A. C. Hewson, J. Bauer, and W. Koller, *Phys. Rev. B* **73**, 045117 (2006).
- ³⁹J. Bauer and A. C. Hewson, *Phys. Rev. B* **76**, 035119 (2007).
- ⁴⁰J. Bauer, A. C. Hewson, and A. Oguri, *J. Magn. Magn. Mater.* **310**, 1133 (2007).
- ⁴¹R. Zitko, R. Peters, and T. Pruschke, *New J. Phys.* **11**, 053003 (2009).
- ⁴²R. Zitko, e-print arXiv:1105.4693.
- ⁴³C. H. L. Quay, J. Cumings, S. J. Gamble, R. de Picciotto, H. Kataura, and D. Goldhaber-Gordon, *Phys. Rev. B* **76**, 245311 (2007).
- ⁴⁴T.-M. Liu, B. Hemingway, A. Kogan, S. Herbert, and M. Melloch, *Phys. Rev. Lett.* **103**, 026803 (2009).
- ⁴⁵S. Schmitt and F. B. Anders, *Phys. Rev. Lett.* **107**, 056801 (2011).
- ⁴⁶A. C. Hewson, J. Bauer, and A. Oguri, *J. Phys. Condens. Matter* **17**, 5413 (2005).
- ⁴⁷F. B. Anders and S. Schmitt, *J. Phys.: Conf. Ser.* **220**, 012021 (2010).
- ⁴⁸F. B. Anders, *Phys. Rev. Lett.* **101**, 066804 (2008).

- ⁴⁹A. Weichselbaum and J. von Delft, *Phys. Rev. Lett.* **99**, 076402 (2007).
- ⁵⁰R. Peters, T. Pruschke, and F. B. Anders, *Phys. Rev. B* **74**, 245114 (2006).
- ⁵¹W. C. Oliveira and L. N. Oliveira, *Phys. Rev. B* **49**, 11986 (1994).
- ⁵²R. Bulla, A. C. Hewson, and T. Pruschke, *J. Phys. Condens. Matter* **10**, 8365 (1998).
- ⁵³J. R. Schrieffer and P. A. Wolff, *Phys. Rev.* **149**, 491 (1966).
- ⁵⁴P. Nozières and A. Blandin, *J. Phys. (France)* **41**, 193 (1980).
- ⁵⁵P. Mehta, N. Andrei, P. Coleman, L. Borda, and G. Zarand, *Phys. Rev. B* **72**, 014430 (2005).
- ⁵⁶N. Andrei, K. Furuya, and J. H. Lowenstein, *Rev. Mod. Phys.* **55**, 331 (1983).
- ⁵⁷ T_K is the $h = 0$ Kondo scale, defined²⁴ for the AIM by $S_{\text{imp}}(T_K) = 0.1$ with $S_{\text{imp}}(T)$ the dot (impurity) contribution to the entropy of the system.
- ⁵⁸We define²⁴ $T_K^{S=1}$ by $S_{\text{imp}}(T_K^{S=1}, h = 0) = 0.8$, suitably between $\ln 2$ and $\ln 3$.
- ⁵⁹K. Furuya and J. H. Lowenstein, *Phys. Rev. B* **25**, 5935 (1982).
- ⁶⁰H. Zhang, X. C. Xie, and Q.-f. Sun, *Phys. Rev. B* **82**, 075111 (2010).
- ⁶¹W. Koller, A. C. Hewson, and D. Meyer, *Phys. Rev. B* **72**, 045117 (2005).
- ⁶²The bandwidth D is taken to be sufficiently larger than all other energies so that its precise value is immaterial.
- ⁶³D. E. Logan, M. P. Eastwood, and M. A. Tusch, *J. Phys. Condens. Matter* **10**, 2673 (1998).
- ⁶⁴N. E. Bickers, *Rev. Mod. Phys.* **59**, 845 (1987).
- ⁶⁵D. E. Logan and M. R. Galpin, *J. Chem. Phys.* **130**, 224503 (2009).